Self-organization of magnetic nanoparticles: A Monte Carlo study

J. Richardi* and M. P. Pileni†
Laboratoire des Matériaux Mésoscopiques et Nanométriques, UMR CNRS 7070, Université Pierre et Marie Curie (Paris VI), Boîte Postale 52, 4, place Jussieu, 75230 Paris Cedex 05, France

J.-J. Weis‡
Laboratoire de Physique Théorique, UMR 8627, Université de Paris XI, Bâtiment 210, 91405 Orsay Cedex, France
(Received 1 February 2008; published 25 June 2008)

To understand the self-organization of magnetic nanocrystals in an applied field, we perform Monte Carlo simulations of Stockmayer fluids confined between two parallel walls. The system is examined in the gas-liquid coexistence region of its phase diagram and the field is applied perpendicular to the walls. Gibbs ensemble simulations are carried out to determine the phase coexistence curves of the confined Stockmayer fluid. In canonical simulations, different types of organizations appear dependent on particle density: columns, walls, and elongated and spherical holes. The morphology and size of structures are in good agreement with results obtained by free energy minimization and experiments. The influence of a distribution of particle sizes on the particle organization is investigated.

DOI: 10.1103/PhysRevE.77.061510 PACS number(s): 83.80.Gv, 47.54.−r, 47.65.Cb, 77.84.Nh

I. INTRODUCTION

The self-organization of nanoparticles is widely used to fabricate well-defined structures at the nanometric and mesoscopic scales [1]. The study of these assemblies shows that they have new intrinsic properties that correspond to neither those of the bulk nor those of individual particles. Thus, tailored materials with new properties can be developed which may be important for applications and fundamental research. The use of magnetic nanoparticles is of great interest, since their organization can be altered by an externally applied magnetic field. Thus, when a field is applied perpendicular to the substrate during the evaporation of a solution of magnetic nanoparticles, labyrinthine patterns and hexagonal arrays of columns of submicrometer dimensions are observed at the end of evaporation [2–5]. Similar structures were previously obtained in ferrofluid systems [6–11]. A free energy approach was recently developed to understand the hexagonal and labyrinthine organizations of magnetic nanoparticles [12,13]. The pattern formation is explained by a minimization of the free energy, which is described by a sum of the energy necessary to create the surface of the structures and the repulsive energy between the aligned magnetic dipoles. Based on the comparison between experiment and theory [4,5] the following mechanism of pattern formation was proposed. During the evaporation process the increase in nanocrystal concentration leads to a phase transition, forming a colloidal gas and liquid phase within the solvent layer. The first phase is a diluted nanocrystal solution, whereas the second one is a highly concentrated solution. Both phases coexist and the patterns are formed by the concentrated phase before the end of evaporation. The free energy approach correctly describes the evolution of the patterns with field strength, pattern height, and surface coverage [4,5].

Here, we perform Monte Carlo (MC) simulations of the self-organization of magnetic nanoparticles in an external field. The aim is to study three fundamental questions which seem difficult to answer by free energy approaches. First, the free energy approaches usually assume idealized predefined structures to find the energy minimum. This restriction is not necessary in simulations where structures are free to evolve according to the imposed external conditions. In particular, by varying the external field strength one can investigate possible transitions between hexagonal and labyrinthine structures. Such transitions were observed experimentally, but were not found by the free energy approach [12]. Second, in the literature several free energy models were proposed to take into account the entropy due to the particle aggregation [12,14,15]. Thus, the entropy is approximated by that of a lattice gas, that of a fluid described by the Carnahan-Starling equation of state [16], or that of a number of distinguishable aggregates. The results, such as the phase diagram and the pattern size, depend sensitively on the entropy approximation. MC simulations, on the other hand, accurately include entropy and comparison of simulation and free energy results can thus reveal the importance of entropy for organization. Finally, recent experiments raised the question of the influence of particle size polydispersity on pattern morphology [17]. Thus, columns were found to be mainly produced when the size distribution is rather low (13%), whereas labyrinths are formed at higher polydispersity (17%). It is difficult to introduce particle properties such as the size distribution into a macroscopic free energy approach, while in simulations the polydispersity can be easily implemented.

In our simulations, a Stockmayer fluid is confined between two parallel walls and a magnetic field is applied perpendicular to the walls. Since pattern formation is experimentally associated with a gas-liquid transition, the parameters of the system were chosen within the gas-liquid coexistence region of the Stockmayer fluid. The latter was chosen for convenience since its properties have been widely studied [18–22]; in particular, the phase diagram of the bulk and its dependence on an external magnetic field are known [21].

*johannes.richardi@upmc.fr; http://www.sri.jussieu.fr
†pileni@sri.jussieu.fr; http://www.sri.jussieu.fr
‡Jean-Jacques.Weis@th.u-psud.fr

The paper is organized as follows. In Sec. II the interaction model and the simulation method are described. In Sec. III, the phase diagram and the magnetization curves of the Stockmayer fluid confined between two walls are studied in order to choose values for the density, temperature, and magnetic field strength within the gas-liquid coexistence region. The properties and structures obtained at varying field strengths, densities, and wall separations are discussed. In Sec. III D, the results are compared to those from free energy approaches. Finally, the size distribution of the particles is varied from 0 to 20% to obtain first indications of the influence of this parameter on the particle organization. Section IV contains the conclusions.

II. SIMULATION METHOD

A. Interaction model

The interaction between two nanoparticles i and j is described by a Stockmayer pair potential, which consists of a dipole-dipole (DD) interaction $v_{\mathrm{DD}}(\boldsymbol{r}_{ij},\boldsymbol{\mu}_i,\boldsymbol{\mu}_j)$ and a Lennard-Jones (LJ) potential $v_{\mathrm{LJ}}(r_{ij})$:

$$v_{\mathrm{LJ}}(r_{ij}) = 4\varepsilon\left[\left(\frac{\sigma}{r_{ij}}\right)^{12} - \left(\frac{\sigma}{r_{ij}}\right)^{6}\right], \tag{1}$$

$$v_{\mathrm{DD}}(\boldsymbol{r}_{ij},\boldsymbol{\mu}_i,\boldsymbol{\mu}_j) = \frac{1}{4\pi\mu_0 r_{ij}^3}\left(\boldsymbol{\mu}_i\cdot\boldsymbol{\mu}_j - \frac{3(\boldsymbol{\mu}_i\cdot\boldsymbol{r}_{ij})(\boldsymbol{\mu}_j\cdot\boldsymbol{r}_{ij})}{r_{ij}^2}\right), \tag{2}$$

where $\boldsymbol{\mu}_i$ and $\boldsymbol{\mu}_j$ are the dipole moments of particles i and j, $\boldsymbol{r}_{ij}=\boldsymbol{r}_j-\boldsymbol{r}_i$ the vector joining the centers of mass of the particles, and $r_{ij}=|\boldsymbol{r}_{ij}|$. The LJ term, truncated here at $r_c=3.2\sigma$, models the van der Waals attraction which leads to an isotropic gas-liquid transition.

A value of 10 nm is chosen for σ, which is typical for the cobalt nanocrystals experimentally used [4]. The magnetic dipole is calculated from the bulk magnetization M_d and the magnetic diameter d_m of the particle using

$$\mu = \mu_0 M_d(\pi/6)d_m^3, \tag{3}$$

where $\mu_0=4\pi\times10^{-7}$ J A^{-2} m^{-1} is the permeability of vacuum.

The magnetic diameter is usually smaller than the size σ of the nanocrystals, e.g., due to the coating molecules surrounding the particles. $M_d=14\times10^5$ A m^{-1} and $d_m=8$ nm are chosen, close to the values for the cobalt nanocrystals employed in the experiments [4]. Reduced units are used throughout the paper: $T^*=kT/\varepsilon$, $\rho^*=\rho\sigma^3$, $\mu^*=\mu/\sqrt{(4\pi\mu_0\varepsilon\sigma^3)}$, and $H^*=H\sqrt{\sigma^3\varepsilon}$, where T, ρ, μ, and H denote the temperature, number density, dipole moment, and applied field strength, respectively. Distances are expressed in units of σ. The reduced temperature T^* is fixed at 1.25 which corresponds to a value $\varepsilon=0.331\times10^{-20}$ J at $T=300$ K. This leads to the following parameters for the Stockmayer fluid studied here: $\mu=2.0$, $T=1.25$, $\sigma=1.0$, $\rho=0.1-0.5$ (for notational convenience the asterisks will be omitted in the following).

In order to model the thin film which appears during the evaporation of the nanoparticle solution, the Stockmayer fluid is confined between two parallel walls separated by a distance L. The particle-wall interaction is given by a purely repulsive (reduced) potential

$$u_{iw} = \frac{1}{(z_i - z_w)^{12}}, \tag{4}$$

where z_i is the z coordinate of particle i. z_w denotes the position of the two walls located at $z_w=-L/2$ and $L/2$, respectively. In this study, the height is usually fixed at $L=10$. To examine the influence of the height on the particle organization, additional simulations were carried out at $L=4$, 6, and 18. The heights in the experiments in Ref. [4] vary between 0.2 and 25 μm. So the heights between 0.05 and 0.18 μm used here are at the lower limit of the experimental range.

The polydispersity of the particle size was described by a Gaussian function as in the experiments [17]:

$$P(\sigma) = \frac{e^{-(\sigma-\bar{\sigma})^2/2v^2}}{v\sqrt{2\pi}}, \tag{5}$$

where $\bar{\sigma}$ denotes the mean diameter (chosen as the unit of length) of the particles and v the variance. Sampling of the particle size according to this Gaussian distribution can be made in various ways. A first one is to choose two uniform random numbers ξ_1 and ξ_2 in [0,1] and calculate $r=(-2\ln\xi_1)^{1/2}\cos(2\pi\xi_2)$. A random diameter generated from the distribution (5) is then given by $\sigma=\bar{\sigma}+vr$ [23,24]. An alternative is to use the rejection method valid for an arbitrary distribution [24]. A third, nonrandom, way is to integrate the Gaussian function in Eq. (5) over the interval σ_i and $\sigma_i+\delta\sigma_i$ where $\delta\sigma_i$ is chosen such that the integral is equal to $1/N$ where N is the number of particles. Then, the value $\sigma_i+0.5\delta\sigma_i$ is attributed as particle size to particle i. The method starts from $\sigma_1=\bar{\sigma}$. The next values of σ_i are given by $\sigma_i=\sigma_{i-1}+\delta\sigma_i$. Particle sizes smaller then $\bar{\sigma}$ are obtained by symmetry.

The variance $v=0.1$ corresponds to a polydispersity of 10% and yields particle sizes ranging from 0.60 to 1.35. According to Eq. (3), we can assume that the dipole moment scales with the cube of the particle diameter: $\mu_i=(\sigma_i/\bar{\sigma})^3\mu$, where $\mu=2.0$. The LJ attraction described by the ε value is assumed not to change with particle size. We have checked that all techniques to sample the particle size yield the same results within the statistical accuracy of the simulations. The density is defined as the number of particles per volume. Please note that in a polydisperse system as defined here the packing fraction is larger than in a monodisperse one. This is related to the fact that the particle volume increases with the cube of the particle diameter. Thus, for the monodisperse system the packing fraction is $\eta=(\pi/6)\rho$, while for a polydispersity of 10% and 20% it is $\eta=1.03(\pi/6)\rho$ and $1.12(\pi/6)\rho$ ($\rho=\frac{N}{V}\bar{\sigma}^3$), respectively.

B. Details of the simulation procedure

Canonical ensemble (NVT) MC simulations were performed with number of particles between $N=1000$ and 3000 [23]. Although both system sizes gave similar qualitative

structures, the advantage of the larger system size is that organized structures, such as, for instance, arrays of columns, could be visualized over a larger region of space. For the confined system, periodicity of the system in the x and y directions is assumed whereas for the bulk system periodicity applies in all three spatial directions.

The most appropriate way to deal with the long-range dipolar interaction in simulations involving, necessarily, a finite number of particles is to repeat the central simulation cell periodically in space and to perform an Ewald sum [23,25]. This method can be conveniently applied to three-dimensional (3D) bulk systems, but less so for the slab geometry considered in the present work where periodicity occurs only in two spatial directions. Although rigorous expressions for the Ewald sums in this geometry are available (see, e.g., Refs. [26–28]), they, unfortunately, are impractical for use in extensive simulation studies as they lead to large computational costs. To bypass this drawback, an alternative is to enforce periodicity in three dimensions by considering an infinite number of parallel slabs separated by vacuum and applying the convential 3D Ewald method [29,30]. If the region of empty space is sufficiently large the interaction between periodic images of the slab is expected to become negligible. In practice, the slab of particles is enclosed in a cuboidal simulation cell of dimensions L_x, L_y, L_z (with $L_x = L_y$) where the dimension L_z perpendicular to the slab is much larger than the slab height L. Periodic boundary conditions are then applied in all three directions. If the total dipole moment of the slab in the perpendicular direction $M_z = \Sigma_i \mu_i^z$ is nonzero, contributions from image cells in the z direction can be eliminated (approximately) by supplementing the usual 3D Ewald sum (with conducting boundary conditions) with a correction term $2\pi M_z^2 / V_{\text{cell}}$, where $V_{\text{cell}} = L_x L_y L_z$ is the volume of the simulation cell [31–33].

The Ewald expression for the energy of the fully periodic 3D system of N dipolar particles is then given by [23,31,34]

$$E = \frac{1}{2}\sum_{i,j=1}^{N}{\sum_{\boldsymbol{n}}}' \frac{1}{|\boldsymbol{r}_{ij}+\boldsymbol{t}\cdot\boldsymbol{n}|^3}\left(\boldsymbol{\mu}_i\cdot\boldsymbol{\mu}_j B(\alpha|\boldsymbol{r}_{ij}+\boldsymbol{t}\cdot\boldsymbol{n}|) - 3\frac{\boldsymbol{\mu}_i\cdot(\boldsymbol{r}_{ij}+\boldsymbol{t}\cdot\boldsymbol{n})\boldsymbol{\mu}_j\cdot(\boldsymbol{r}_{ij}+\boldsymbol{t}\cdot\boldsymbol{n})}{|\boldsymbol{r}_{ij}+\boldsymbol{t}\cdot\boldsymbol{n}|^2} C(\alpha|\boldsymbol{r}_{ij}+\boldsymbol{t}\cdot\boldsymbol{n}|)\right) + \frac{2\pi}{V_{\text{cell}}}\sum_{i,j=1}^{N}\sum_{\boldsymbol{G}\neq\boldsymbol{0}} e^{-G^2/(4\alpha^2)}\frac{(\boldsymbol{\mu}_i\cdot\boldsymbol{G})(\boldsymbol{\mu}_j\cdot\boldsymbol{G})}{G^2}\exp(i\boldsymbol{G}\cdot\boldsymbol{r}_{ij}) - \frac{2\alpha^3}{3\sqrt{\pi}}\sum_{i=1,\ldots,N}\boldsymbol{\mu}_j^2 + \frac{2\pi}{V_{\text{cell}}}M_z^2. \tag{6}$$

The prime in the sum over $\boldsymbol{n} = (n_x, n_y, n_z)$ (n_x, n_y, n_z integers) means that the term $i=j$ is omitted for $\boldsymbol{n}=\boldsymbol{0}$. The parameter α regulates the relative convergence of the sums in direct, r, and reciprocal, k, space,

$$\boldsymbol{t} = \begin{pmatrix} L_x & 0 & 0 \\ 0 & L_y & 0 \\ 0 & 0 & L_z \end{pmatrix} \tag{7}$$

is the cell matrix, and $B(r)$ and $C(r)$ are given by

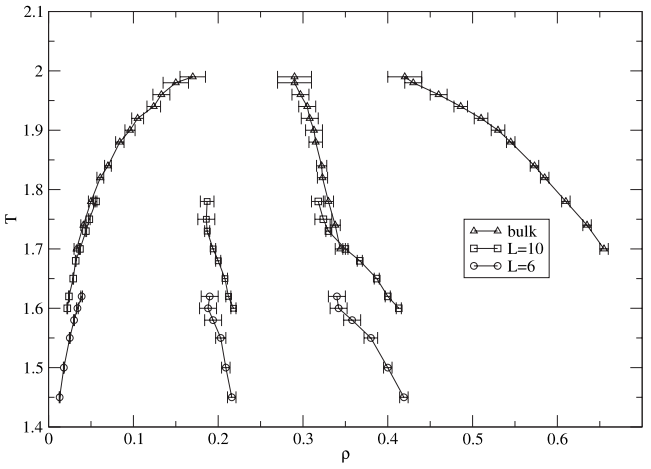

FIG. 1. Coexistence curves calculated in the Gibbs ensemble simulations for the bulk and confined Stockmayer fluid ($\mu=2.0$). The triangles (bulk), squares ($L=10$), and circles ($L=6$) are the coexisting densities found in the simulations. The lines serve as a guide to the eyes. The lines between the coexisting curves correspond to the values of $(\rho_g+\rho_l)/2$.

$$B(r) = \text{erfc}(\alpha r) + \frac{2\alpha r}{\sqrt{\pi}}\exp(-\alpha^2 r^2) \tag{8}$$

and

$$C(r) = \text{erfc}(\alpha r) + \frac{2\alpha r}{\sqrt{\pi}}\exp(-\alpha^2 r^2)\left(1+\frac{2}{3}\alpha^2 r^2\right) \tag{9}$$

with erfc(x) the complementary error function [23]. The reciprocal lattice vectors are given by $\boldsymbol{G} = (\frac{2\pi}{L_x}n_x, \frac{2\pi}{L_y}n_y, \frac{2\pi}{L_z}n_z)$. Vectors satisfying $\boldsymbol{n}^2 \leq 64$ were included in the sum. The parameter α was chosen sufficiently large to consider only interactions within the central simulation box in the real space contributions. L_z was taken as $(3-4)L$. Typical canonical calculations involved $(0.5-2)\times 10^6$ ($N=1000$) and $(0.2-0.8)\times 10^6$ ($N=2592$, 3000) cycles, a cycle corresponding to translation and rotation of the N particles.

III. RESULTS

A. Gas-liquid phase coexistence of a confined Stockmayer fluid

As stated in the Introduction, our aim is to perform simulations at state points inside the gas-liquid coexistence region for the confined Stockmayer fluid. Therefore, the coexistence curves were determined using Gibbs ensemble Monte Carlo (GEMC) simulations [25,35] using a total of 1000 particles. Typical runs involved between 4×10^6 and 10×10^6 cycles depending on temperature, each cycle corresponding to translation and rotation of the N particles, one volume change, and N particle exchanges. During a change of the system volume $V = L_x L_y L$, the wall separation L is kept constant.

Figure 1 shows the coexistence curves for the bulk and two different wall separations $L=6$ and 10. The critical temperature and density of the bulk are approximately $T_c = 2.0$ and $\rho_c = 0.29$. As GEMC simulations give rather large error

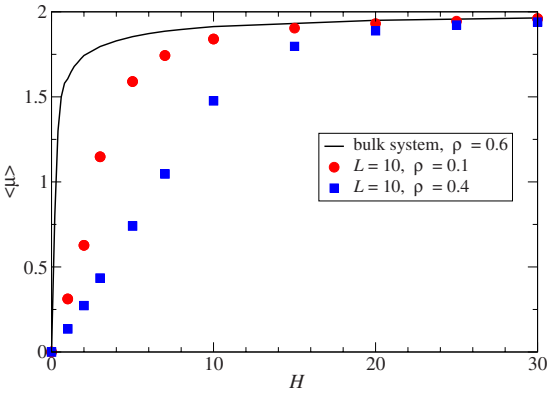

FIG. 2. (Color online) Magnetization calculated in canonical Monte Carlo simulations for the bulk and confined Stockmayer fluid (σ=1.0, T=1.25, μ=2.0). The height of the confined system is L=10.

bars in the critical region and no finite-size effects were studied, we did not attempt to do a more precise location of the critical point. The results are in agreement with those of van Leeuwen *et al.* [19] (T_c=2.06, ρ_c=0.289), Stoll *et al.* [36] (T_c=2.062, ρ_c=0.2961), and Stevens and Grest [21] (T_c=2.08, ρ_c=0.28; values taken from their Fig. 1). The lower value of T_c found in our study results from the truncation of the LJ part of the Stockmayer potential at r_c=3.2. No long-tail correction has been added (see, e.g., Ref. [37]).

As shown in Fig. 1, confinement of the Stockmayer fluid between two parallel walls leads to a narrowing of the coexistence region and a marked decrease of the critical temperature and density. The critical point for L=10 is approximately T_c=1.8,ρ_c=0.2, and T_c=1.7,ρ_c=0.2 for L=6. The smaller T_c is the consequence of a lower attractive energy per particle due to the truncation by the walls.

As shown by Stevens and Grest [21], applying an external field to the bulk Stockmayer fluid leads to an increase of the critical temperature while the density changes only slightly, at least at low field strength ($H \leq 5$), as a result of the stronger dipole attractions in the presence of the field. They are caused by the alignment of dipoles with the field direction which leads to a correlation of dipole moments. We were able to reproduce this trend for the bulk system but did not succeed in achieving phase coexistence of the confined fluid in an applied field in the GEMC simulations except at very low field. One can note that attractive interactions are diminished both by lowering L and by increasing the field strength, which ultimately impedes formation of gas-liquid coexistence. The increase of repulsive forces is at the origin of pattern formation.

The chosen reduced temperature T=1.25 is significantly lower than the critical temperatures of the confined systems and guarantees that most simulations are carried out in a region where liquid and gas can coexist.

B. The magnetization curve of a confined Stockmayer fluid

To determine appropriate field strengths for the simulations, the magnetization as a function of field is computed by simulation [38]. Figure 2 shows that the average magnetization for a confined Stockmayer fluid at ρ=0.1 and 0.4 are significantly smaller than that of a bulk system due to the appearance of a strong demagnetization field at the walls [13]. The magnetization of the bulk system is calculated at ρ=0.6, which corresponds to the density within the clusters found at ρ=0.1 and 0.4 for the confined system. In view of these results the confined systems were studied at the field strengths H=0, 1, 3, 5, 10, 30, which correspond to 0, 0.018, 0.054, 0.090, 0.18, and 0.545 T, respectively.

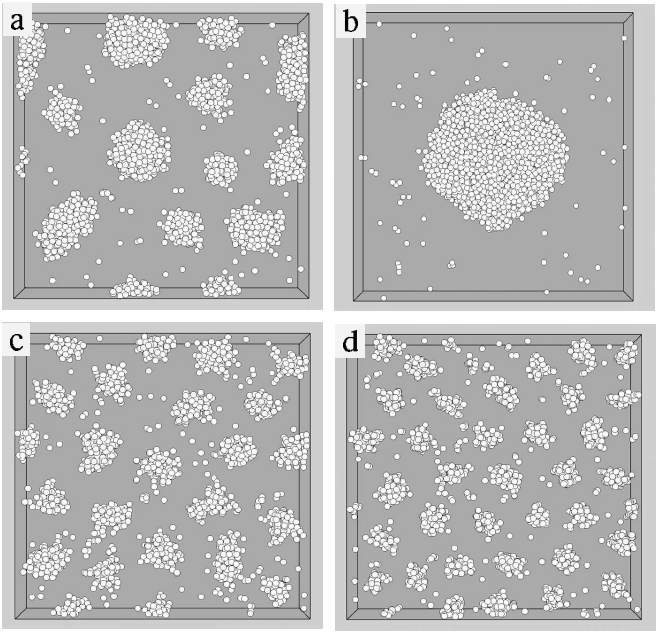

FIG. 3. Snapshots of configurations for a confined Stockmayer fluid at T=1.25, μ=2.0, ρ=0.1, and L=10. H= (a),(b) 1, (c) 5, and (d) 30. Configuration (a) is obtained from a random initial configuration while the simulation of (b) is started from a central concentrated phase (see text for details). In (a), (c), and (d) N=2592; in (b) N=3000.

C. Particle organizations at a height L=10

In this section we describe the particle organization obtained from simulation for a wall separation L=10. To examine the influence of initial conditions on the final particle arrangement the simulations at ρ=0.1 were started from several different initial configurations: (α) random positions and random orientations of the dipole moments of the particles, (β) positions on a regular lattice and random orientations of the dipole moments, (γ) configuration at a given field strength used as input at a higher field, and (δ) particles initially concentrated in a cylinder with density ρ=0.6 (the density inside the final droplets) in the middle of the simulation cell.

At low field strength (H<3) typical structures at ρ=0.1 obtained with conditions $\alpha-\gamma$ consisted of several droplets of average radius $\approx$7 [Fig. 3(a)]. On the other hand the initial condition δ appeared to be rather stable and did not evolve much over the "time" span of the simulation [Fig. 3(b)]. In contrast, at $H \geq 5$, any initial configuration $\alpha-\delta$ gave similar final structures. The reason is an increase of the

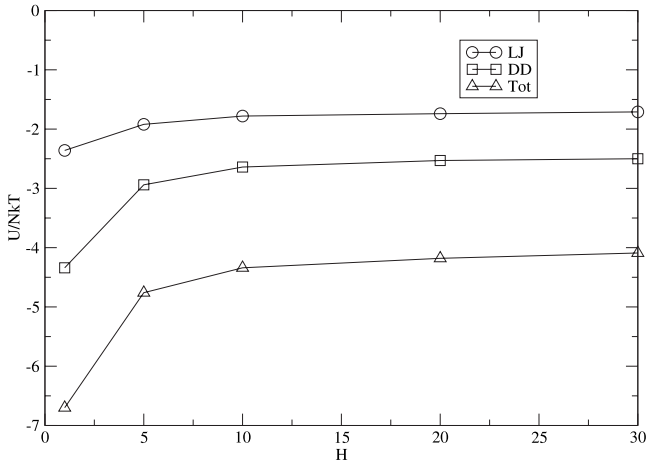

FIG. 4. Total internal energy and its Lennard-Jones and dipole-dipole contributions as a function of the magnetic field strength H for a confined Stockmayer fluid (T=1.25, μ=2.0, ρ=0.1, and L=10).

dipolar repulsion, as apparent in Fig. 4 showing the variation with H of the LJ and dipole-dipole contributions to the energy. The final organizations at H=5 and 30 in Figs. 3(c) and 3(d) can be described as assemblies of columns with height L and radius r_0. Figure 5(a) shows a tilted view of the structure obtained at ρ=0.1 and H=30.

An enumeration of clusters has been made using a proximity criterion: a particle belongs to a cluster if its distance to any other particle of the cluster is smaller than r_c=1.5 (results are relatively insensitive to neighboring values). As shown in Fig. 6 the average number of clusters increases with field strength (as also apparent on the snapshots of configurations of Fig. 3) and concomitantly the average radius of the columns decreases (cf. Fig. 7) in good agreement with experiment and theory [4,5,12,14]. A more detailed comparison with the free energy results will be carried out below in Sec. III D. It should be noted that the columns arrange only approximately in the hexagonal array often observed in experiments [4]. Some deviation from a perfect hexagonal order is explained by the fact that such an organization has to

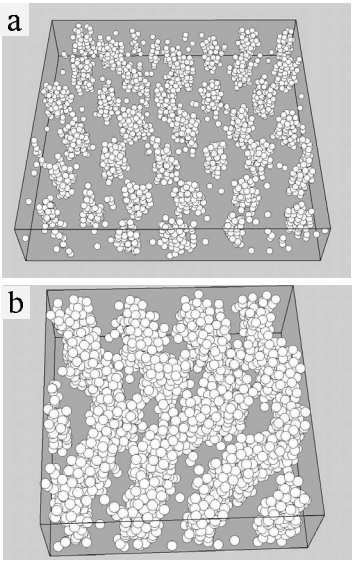

FIG. 5. Tilted view of configurations for the confined Stockmayer fluid at T=1.25, μ=2.0, H=30, and L=10: ρ= (a) 0.1 and (b) 0.3.

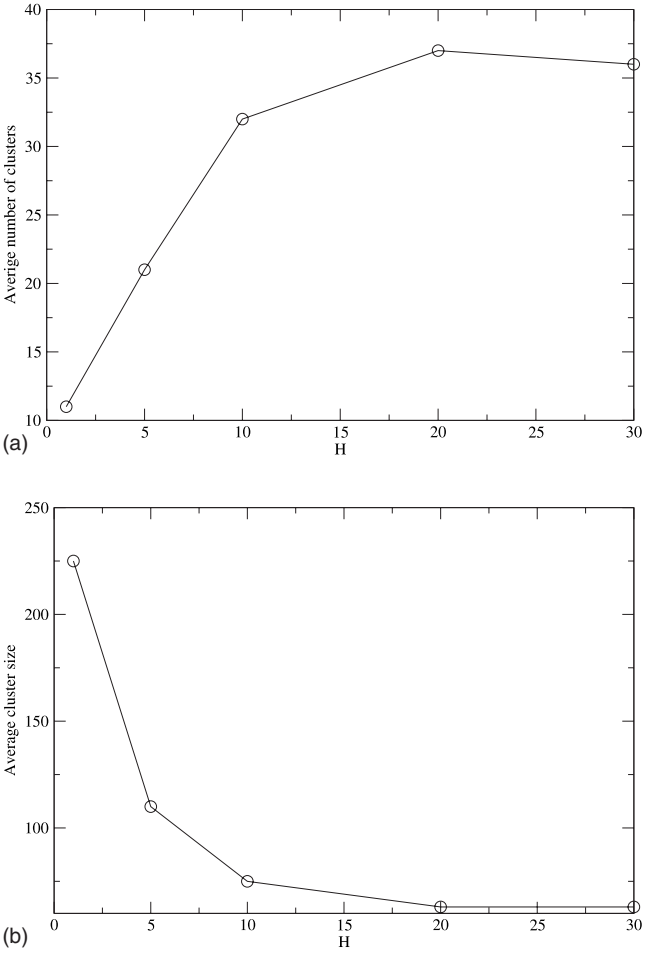

FIG. 6. Average number of clusters (a) and their size (b) as a function of the magnetic field strength H for a confined Stockmayer fluid (T=1.25, μ=2.0, ρ=0.1, and L=10).

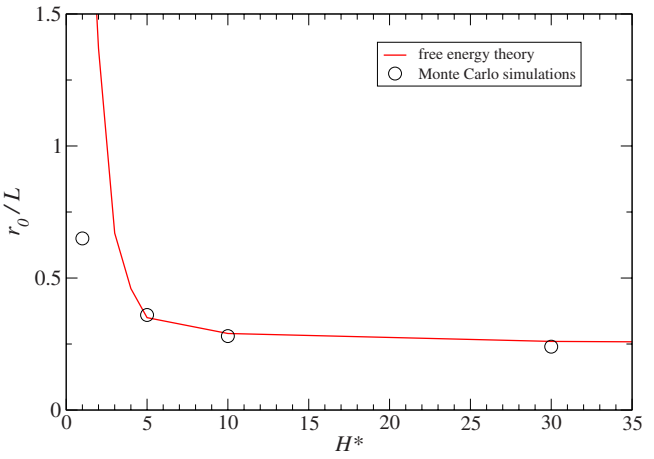

FIG. 7. (Color online) Evolution of the average column radius for ρ=0.1. Comparison of simulation and free energy results.

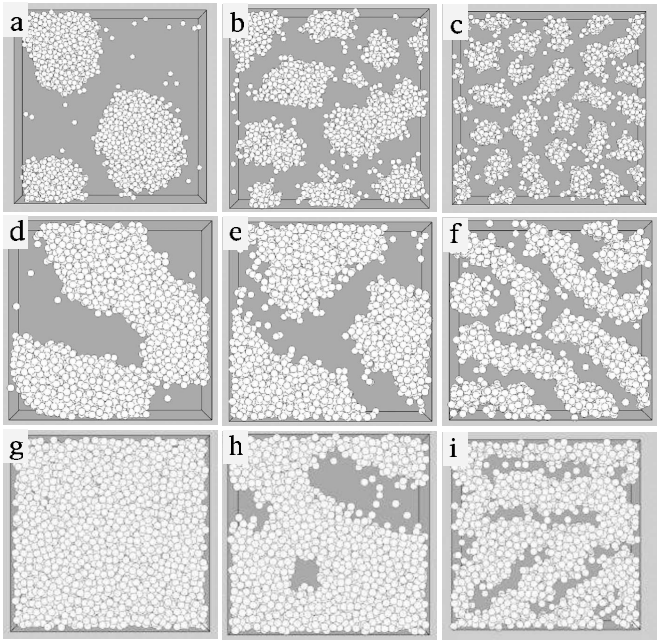

FIG. 8. Snapshots of configurations for a confined Stockmayer fluid at $T=1.25$, $\mu=2.0$, and $L=10$: (a)–(c) $\rho=0.2$, $H=1$, 5, and 30; (d)–(f) $\rho=0.3$, $H=1$, 5, and 30; (g)–(i) $\rho=0.4$, $H=1$, 5, and 30. $N=3000$ except for (d)–(f) where $N=2592$.

fit to the periodic boundary conditions applied to our simulation box. Some local disorder is due to the inhomogeneous size and form of the columns. In experiments as well, a distortion of the hexagonal structures is observed when the columns are not well defined, as seen in the inset of Fig. 2c in Ref. [4].

Let us now examine how the structures evolve when the density increases. At $\rho=0.2$ and $H=1$, slightly elongated droplets are found [Fig. 8(a)]. At $H=5$ and 30 [Figs. 8(b) and 8(c)], columns appear which sometimes connect to form elongated structures, signaling the formation of sheet structures observed at somewhat higher densities. Actually, at $\rho=0.3$, the sheet structure (which for much larger system sizes would result in a labyrinthine pattern) predominates at any field as seen in Figs. 8(d)–8(f). The structures are characterized by continuous walls as seen in the tilted view of the structure obtained at $\rho=0.3$ and $H=30$ in Fig. 5. The particle distribution $\rho(z)$ perpendicular to the walls is shown in Fig. 9 for $H=1$ and 20. Particles are seen to be pushed away by about 0.5σ from each repulsive wall so that the effective density of the system is approximately 0.375. From Fig. 9, it is also recognized that at $H=1$ the density of the droplets is maximum in the middle of the simulation box and decreases toward the walls while in the labyrinth phase ($H=20$) the density is highest near the walls and decreases in an oscillatory fashion toward the center of the box, where it is roughly equal to the effective density of the system. At small field strengths, the surfaces delimiting the clusters perpendicular to the two walls are curved. Therefore, more particles are in the middle than close to the walls. At $H=20$, a sheet structure is formed. The surfaces delimiting the sheets are straight in the direction perpendicular to the walls and, therefore, the density in the center of the box is roughly equal to the effective density of the system. The oscillations of the profile are induced by the presence of the wall. It shows a structuring within the aggregates leading to an assembly of particle chains perpendicular to the walls. The appearance of labyrinthine structures at higher densities is in agreement with prediction from free energy approaches [12,15]. In Ref. [12], a transition from columns to labyrinth is obtained between $\phi=0.3$ and 0.4, where ϕ is the ratio between the liquid and the total volume fractions. In simulations, the ratio ϕ is related to the density by the equation $\phi=\rho L/\rho_l(L-\sigma)$, where we take into account that a layer of thickness 0.5 between the fluid and the wall is not accessible to the particles (see Fig. 9). The density ρ_l inside the liquid phase is found to be approximately 0.6. This leads to a volume fraction $\phi=0.37$ at $\rho=0.2$ where the transition starts to be observed, in good agreement with the free energy approaches. At $\rho=0.4$ [Figs. 8(g)–8(i)], a closed film is found at low field strengths. At higher fields, new structures appear: elongated holes in the liquid film appear at $\rho=0.4$. At even higher densities ($\rho>0.5$, not shown here) the holes take a cylindrical shape, arranging in a distorted hexagonal array. This organization corresponds to the inverted hexagonal structure predicted by the free energy approach of Ref. [15]. In an upcoming presentation [39], these structural results will be compared to recent experiments.

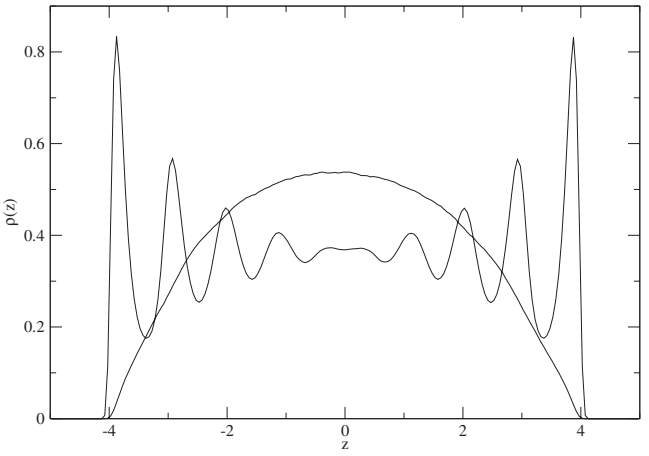

FIG. 9. Particle density distribution $\rho(z)$ perpendicular to the walls at $H=1$ and 20 (structured curve) for a confined Stockmayer fluid ($T=1.25$, $\mu=2.0$, $\rho=0.3$, and $L=10$).

D. Comparison with free energy results

The radii of the columns obtained from simulations are compared here to predictions from the free energy approach. The free energy of the system is described as a sum of surface and magnetic terms. Free energy theories which take only the magnetic and surface energies into account neglect the change in entropy due to the transitions of the particles from a free to an aggregated state. Several attempts have been made in the literature to take this entropy change into account. Since an accurate approximation of the entropy due to the aggregation is not yet available, it will be neglected here. Please note that some entropy, but not directly related to the particle aggregation, is included in the model by the

use of the temperature-dependent magnetization. In a first approach we restrict ourselves to the structures obtained at $\rho=0.1$, which can be well described by a geometrical model of an assembly of cylinders. The surface energy per cylinder is given by

$$F_s = 2\pi r_0(L-2\sigma)\gamma, \tag{10}$$

where $2\pi r_0(L-2\sigma)$ is the surface area of the cylinder. The surface of the cylinder corresponds to the average position of the outermost particles in the columns. The interfacial tension γ is approximated by the average LJ energy $v_{\mathrm{LJ},e}$ of the particles at the surface of the columns

$$\gamma = 0.5\rho_l v_{\mathrm{LJ},e}. \tag{11}$$

$v_{\mathrm{LJ},e}$ varies between -3 and -5 and an average value of -4 is used. This gives a surface tension of 4.0×10^{-5} J m^{-2} in SI units. It is remarkable that this value is very close to the interfacial tension of 5.0×10^{-5} J m^{-2} obtained for cobalt nanocrystals by a comparison between the free energy theory and experiments [4]. We conclude that our model gives a fair description of the experimental system. For the calculation of the magnetic energy, we restrict our comparisons to $H\geq5$, where columns of quite homogeneous size are observed in the simulations. Moreover, at these field strengths the size of the columns does not depend on initial conditions within the length of our simulations. In Ref. [13], we have shown that in this region of field saturation the magnetic energy can be calculated by assuming a constant magnetization during the pattern formation. The magnetic energy of a cylinder is then calculated from the repulsion of the magnetic dipoles (see Ref. [12] for details):

$$F_m = \sum_{i=1}^{N_0} \frac{M^2\mu_0}{4\pi}\int dy_1 dz_1 \int dy_i dz_i \left(\frac{1}{\sqrt{(\vec{s}_1-\vec{s}_i)^2}} - \frac{1}{\sqrt{(\vec{s}_1-\vec{s}_i)^2+L^2}}\right). \tag{12}$$

The sum is over all cylinders in the pattern and $\vec{s}_i=(y_i,z_i)$ denotes all points at the top of the cylinder i. The magnetization M is taken from the simulations. All calculations were carried out using the home-made FORTRAN package HEXALAB [40,41].

The column radius is obtained by the minimization of the free energy per surface area. Figure 7 shows excellent agreement between free energy and simulation results at $H\geq5$. The agreement is all the more remarkable in view of the fact that the free energy results do not involve a fit to the simulation values, e.g., by adjusting the interfacial tension. This agreement indicates that the entropy due to the particle aggregation, neglected here, does not play an important role, at least at low densities and high field strengths. This shows the reliability of the free energy approach at these experimental conditions usually employed to fabricate solid mesostructures from magnetic nanoparticle solutions [4,5].

E. The influence of height

To investigate the influence of confinement, simulations were carried out, in addition to $L=10$, at different densities for $L=4$, 6, and 18. Typical structures are shown in Fig. 10 for increasing values of $H=1$, 5, and 30. At the largest height $L=18$, similar structures are observed as for $L=10$. The most conspicuous effect entailed upon lowering the sample height is a rapid dissociation of the droplets present in zero field into smaller, labile aggregates when the field is increased [see Figs. 10(b) and 10(c)]. The aggregates are not characterized by a well-defined shape such as columns or walls. The size of these aggregates decreases with density and by increasing the dipole moment. In fact, for a dipole moment $\mu=3$ practically only isolated particles oriented in the field are observed at densities $\rho=0.1-0.2$ as a result of the increased repulsion of the dipolar interaction.

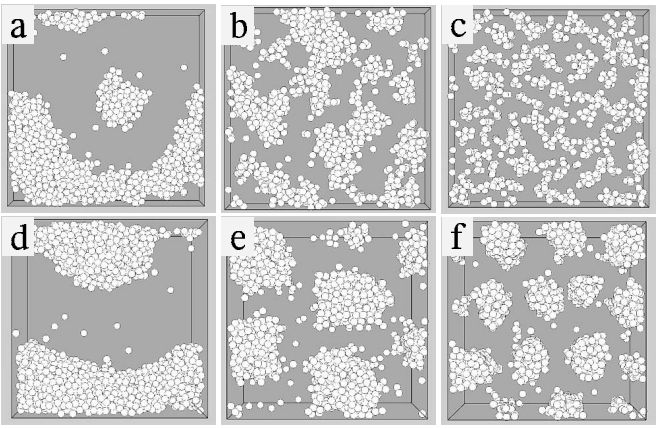

FIG. 10. Snapshots of the configurations for a confined Stockmayer fluid at $T=1.25$, $\mu=2.0$, $\rho=0.2$: $L=$ (a)–(c) 6 and (d)–(f) 18. In (a)–(c) $N=1000$ and in (d)–(f) $N=3000$.

F. The influence of polydispersity

In recent experiments, an indication was found that the size distribution of the nanoparticles may influence the pattern morphology [17]. To corroborate such a possibility simulations were carried out using polydispersities of 10% and 20%. Results were obtained for $L=10$ and 6 at $\rho=0.1$, 0.2, 0.3, and 0.4, $\mu=2$, and field strengths $H=1$, 5, 10, and 30. No appreciable dependence of the structure morphologies on polydispersity is found, at least for the conditions considered here. As an example, Fig. 11 shows the structures obtained at $\rho=0.1$, 0.2, 0.3, and 0.4, $L=10$, for an applied field $H=30$. At high densities of $\rho=0.4$, some differences in the structures [Figs. 11(j)–11(l)] are observed. Thus, the structures are characterized by spherical holes at a polydispersity of 20%, while in the monodisperse case, sheets are found. This may be explained by the higher volume fraction in the polydisperse case due to the presence of larger particles. Thus, the volume fraction increases by 12% for a polydispersity of 20%. In the monodisperse case, at a 12% higher volume fraction corresponding to a number density of 0.45 the formation of spherical holes is also observed [38]. The morphologies observed for 10% (second column) and 20% (third column) polydispersity are quite similar to those for the monodisperse system (first column). The structures obtained for the polydisperse systems seem to be less well defined than in the monodisperse case. Some size segrega-

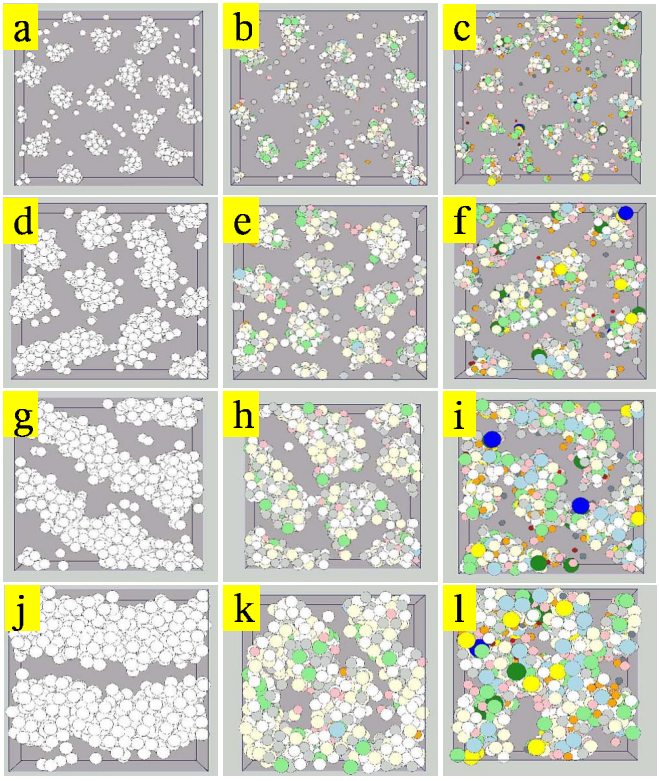

FIG. 11. (Color online) Snapshots of the configurations for a confined Stockmayer fluid at $\bar{\sigma}=1$, $T=1.25$, $\mu=2.0$, $\rho=0.2$, and $L=10$. First column, monodisperse; second column, polydispersity of 10%; third column, polydispersity of 20%. (a)–(c) $\rho=0.1$, (d)–(f) $\rho=0.2$, (g)–(i) $\rho=0.3$, and (j)–(l) $\rho=0.4$. The gray tones (color online) represent particles of different sizes. $N=1000$.

tion is seen to take place during structure formation. Thus the larger particles are found only in the larger clusters, while isolated particles are of the smaller size as also found for the bulk system in Ref. [42]. For the more confined system $L=6$, as for the monodisperse case, the droplets existing in zero field rapidly dissociate into small aggregates when the field increases.

IV. CONCLUSIONS

A Stockmayer fluid confined between two parallel walls is studied by MC simulation as a model system of a cobalt nanocrystal solution evaporating in a field applied perpendicular to the substrate. Pattern formation as a function of field strength is reported for various densities and sample heights at the unique temperature $T=1.25$ and dipole moment $\mu=2$.

In small fields the structure is characterized, for all densities considered ($\rho=0.1-0.5$), by droplets and isolated particles typical of those inside a gas-liquid two-phase region. Transitions to a microphase upon increase of the external field depend on the density. In the density range $\rho=0.1-0.2$ and for $L=10$ a transition to a columnar phase occurs with nearly hexagonal order of the columns. As the field increases, the radius of the more or less cylindrical columns decreases, i.e., in our simulations performed at constant number of particles (between 1000 and 3000), the number of columns increases and the average number of particles in a column decreases. Quite remarkably, the free energy approach described in Sec. III D predicts the dependence of column radius on field strength extremely well.

In the range $\rho=0.3-0.4$, $L=10$, the microphase consists of an assembly of vertical sheets which on a much larger scale would form a labyrinth pattern. No clear indications for a field-induced transition between columns and labyrinths were observed at fixed density. If such a transition exists, it must be limited to a small range of densities between 0.2 and 0.3.

Well-characterized pattern formation requires a sufficiently strong dipolar interaction. A dipole moment such that $\mu^2/T\approx 3.2$ appears to be close to the minimal value.

The formation of different structures such as columns, labyrinths, and holes with increasing densities is in good agreement with results from the free energy theory [12,15]. Thus, the comparison with simulations confirms the reliability of the free energy approach in predicting the pattern morphology and size at high field strengths, even when the entropy due to the particle aggregation is neglected.

Concerning the influence of sample height on pattern formation, an increase of L to 18 did not entail qualitative changes. Similarly, a columnar phase occurs at $\rho=0.1$ in the unconfined system (periodicity in all three space directions; figure not shown; see also Ref. [43]). On the contrary, lowering of L has a more marked effect. Thus, for $L\leq 6$, the droplets present at zero field rapidly dissociate, in a finite field, into small irregular aggregates with no well-defined order. The size of these aggregates decreases with density and sample height. In the limit of a very thin sample (monolayer) the Stockmayer potential reduces, in a strong magnetic field, to the sum of a LJ potential and a repulsive long-range $\frac{1}{r^3}$ potential. As shown by simulation [44] and experimental [45] results, this magnetic monolayer system exhibits microphases similar to those found here (in strong fields). One can note, however, that in these works a much larger dipole moment was used, yielding sharper phases.

Quite remarkably, microphases including circular-shaped clusters, disordered or ordered on a triangular lattice, and striped phases are also found in simulations of 2D simple systems (spherically symmetric potentials) when a *long-range* repulsive potential is in competion with a shorter-range attractive potential [46]. In 3D systems of competing Yukawa potentials, hole structures were observed as well [47]. This strengthens the belief that formation of microphases can to a large extent be understood by the interplay between the long-range repulsive dipolar forces and attractive forces. Similar considerations have been put forward to explain modulated phases in ferrofluids, thin films of magnetic garnets, diblock copolymers, phospholipid monolayers, etc. [48].

In regard to the influence of polydispersity in the range 10%–20% the morphologies of microstructures are found not to differ qualitatively from those of the monodisperse case. This finding does not match experimental results on cobalt nanocrystals, where the size distribution appears to have a major impact on pattern formation [17]. While at low polydispersity (13%) compact columns are observed to self-

organize into a face-centered-cubic (rather than a hexagonal) structure, at larger polydispersity (18%–20%) a significant number of isolated columns fuse together to form wormlike and labyrinth structures. The mechanism of fusion is attributed to creation of defects at the ends of the columns [17]. It is interesting to note that for a size distribution of 22% only labyrinths are formed with cobalt nanocrystals, whereas with γ-Fe_2O_3 nanocrystals only columns are produced [5]. This may be related to the fact that the volume fraction ϕ is restricted to values below 0.1 for these nanocrystals. In contrast, for cobalt nanocrystals ϕ varies between 0.05 and 0.5, where formation of either hexagonal and labyrinthine patterns is expected from theory. We assume that the influence of the polydispersity on the morphology observed for cobalt nanocrystals may be caused by subtle effects, such as a stronger van der Waals attraction between the larger particles compared to the smaller ones, or by an increase in density with the polydispersity of the system.

[1] *Nanocrystals Forming Mesoscopic Structures*, edited by M. P. Pileni (Wiley, Weinheim, 2005).
[2] J. Legrand, A. T. Ngo, C. Petit, and M. P. Pileni, Adv. Mater. (Weinheim, Ger.) **18**, 53 (2001).
[3] G. Leo, Y. Chushkin, S. Luby, E. Majkova, I. Kostic, M. Ulmeanu, A. Luches, M. Giersig, and M. Hilgendorff, Mater. Sci. Eng., C **23**, 949 (2003).
[4] V. Germain, J. Richardi, D. Ingert, and M. P. Pileni, J. Phys. Chem. **109**, 5541 (2005).
[5] A. T. Ngo, J. Richardi, and M. P. Pileni, Langmuir **21**, 10234 (2005).
[6] R. E. Rosensweig, M. Zahn, and R. Shumovich, J. Magn. Magn. Mater. **39**, 127 (1983).
[7] J.-C. Bacri, R. Perzynski, and D. Salin, Endeavour **12**, 76 (1988).
[8] F. Elias, C. Flament, J.-C. Bacri, and S. Neveu, J. Phys. I **7**, 711 (1997).
[9] C.-Y. Hong, I. J. Jang, H. E. Horng, C. J. Hsu, Y. D. Yao, and H. C. Yang, J. Appl. Phys. **81**, 4275 (1997).
[10] J. Liu, E. M. Lawrence, A. Wu, M. L. Ivey, G. A. Flores, K. Javier, J. Bibette, and J. Richard, Phys. Rev. Lett. **74**, 2828 (1995).
[11] M. F. Islam, K. H. Lin, D. Lacoste, T. C. Lubensky, and A. G. Yodh, Phys. Rev. E **67**, 021402 (2003).
[12] J. Richardi, D. Ingert, and M. P. Pileni, Phys. Rev. E **66**, 046306 (2002).
[13] J. Richardi and M. P. Pileni, Phys. Rev. E **69**, 016304 (2004).
[14] F. M. Ytreberg and S. R. McKay, Phys. Rev. E **61**, 4107 (2000).
[15] D. Lacoste and T. C. Lubensky, Phys. Rev. E **64**, 041506 (2001).
[16] N. F. Carnahan and K. E. Starling, J. Chem. Phys. **51**, 635 (1969).
[17] V. Germain and M. P. Pileni, Adv. Mater. (Weinheim, Ger.) **17**, 1424 (2005).
[18] B. Smit, C. Williams, and E. Hendriks, Mol. Phys. **68**, 765 (1989).
[19] M. van Leeuwen, B. Smit, and E. Hendriks, Mol. Phys. **78**, 271 (1993).
[20] M. van Leeuwen, Mol. Phys. **82**, 383 (1994).
[21] M. J. Stevens and G. S. Grest, Phys. Rev. E **51**, 5976 (1995).
[22] J. Bartke and R. Hentschke, Phys. Rev. E **75**, 061503 (2007).
[23] M. P. Allen and D. J. Tildesley, *Computer Simulation of Liquids* (Clarendon, Oxford, 1989).
[24] M. E. J. Newman and G. T. Berkema, *Monte Carlo Methods in Statistical Physics* (Clarendon, Oxford, 1999).
[25] D. Frenkel and B. Smit, *Understanding Molecular Simulation* (Academic, San Diego, 2002).
[26] D. M. Heyes, Phys. Rev. B **49**, 755 (1994).
[27] A. Grzybowski, E. Gwóźdź, and A. Bródka, Phys. Rev. B **61**, 6706 (2000).
[28] J.-J. Weis and D. Levesque, in *Advanced Computer Simulation Approaches for Soft Matter Sciences II*, edited by C. Holm and K. Kremer, Advances in Polymer Science Vol. 185 (Springer, New York, 2005).
[29] J. C. Shelley and G. N. Patey, Mol. Phys. **88**, 385 (1996).
[30] S. H. L. Klapp and M. Schoen, J. Chem. Phys. **117**, 8050 (2002).
[31] I. C. Yeh and M. L. Berkowitz, J. Chem. Phys. **111**, 3155 (1999).
[32] P. S. Crozier, R. L. Rowley, E. Spohr, and D. Henderson, J. Chem. Phys. **112**, 9253 (2000).
[33] A. Arnold and C. Holm, in *Advanced Computer Simulation Approaches for Soft Matter Sciences II* (Ref. [28]).
[34] S. W. de Leeuw, J. W. Perram, and E. R. Smith, Proc. R. Soc. London, Ser. A **373**, 27 (1980).
[35] A. Z. Panagiotopoulos, Mol. Phys. **62**, 701 (1987).
[36] J. Stoll, J. Vrabec, and H. Hasse, Fluid Phase Equilib. **209**, 29 (2003).
[37] W. Shi and J. K. Johnson, Fluid Phase Equilib. **187-188**, 171 (2001).
[38] Z. Wang, C. Holm, and H. W. Müller, Phys. Rev. E **66**, 021405 (2002).
[39] C. Salzemann, I. Lisiecki, J. J. Weis, J. Richardi, and M. P. Pileni (unpublished).
[40] J. Richardi and M. P. Pileni, Eur. Phys. J. E **13**, 99 (2004).
[41] The FORTRAN package HEXALAB is a highly optimized code of about ten thousand statements, which calculate the geometry and energy of magnetic fluid patterns. The kind of pattern is not restricted to hexagonal or labyrinthine ones. HEXALAB was developed by J. Richardi at the LM2N.
[42] T. Kruse, A. Spanoudaki, and R. Pelster, Phys. Rev. B **68**, 054208 (2003).
[43] A. Satoh, R. W. Chantrell, S.-I. Kamiyama, and G. N. Coverdale, J. Colloid Interface Sci. **181**, 422 (1996).
[44] P. J. Camp, Phys. Rev. E **68**, 061506 (2003).
[45] N. Osterman, D. Babič, I. Poberaj, J. Dobnikar, and P. Ziherl, Phys. Rev. Lett. **99**, 248301 (2007).
[46] A. Imperio and L. Reatto, J. Chem. Phys. **124**, 164712 (2006).
[47] A. J. Archer and N. B. Wilding, Phys. Rev. E **76**, 031501 (2007).
[48] M. Seul and D. Andelman, Science **267**, 476 (1995).